JGR Atmospheres

RESEARCH ARTICLE
10.1029/2021JD036251

Special Section:
The COVID-19 pandemic: linking health, society and environment

Effective Radiative Forcings Due To Anthropogenic Emission Changes Under Covid-19 and Post-Pandemic Recovery Scenarios

Xiaochao Yu[1,2], Hua Zhang[2,3], Bing Xie[3,4], Zhili Wang[5], Shuyun Zhao[6], and Defeng Zhao[1]

[1]Department of Atmospheric and Oceanic Sciences & Institute of Atmospheric Sciences, Fudan University, Shanghai, China, [2]State Key Laboratory of Severe Weather, Chinese Academy of Meteorological Sciences, Beijing, China, [3]Collaborative Innovation Center on Forecast and Evaluation of Meteorological Disasters, Nanjing University of Information Science and Technology, Nanjing, China, [4]Laboratory for Climate Studies of China Meteorological Administration, National Climate Center, China Meteorological Administration, Beijing, China, [5]State Key Laboratory of Severe Weather and Key Laboratory of Atmospheric Chemistry of CMA, Chinese Academy of Meteorological Sciences, Beijing, China, [6]Department of Atmospheric Science, School of Environment Studies, China University of Geosciences, Wuhan, China

Abstract With the continuation of the Coronavirus Disease 2019 (Covid-19) pandemic, the impacts of this catastrophe on anthropogenic emissions are no longer limited to its early stage. This study quantitatively estimates effective radiative forcings (ERFs) due to anthropogenic well-mixed greenhouse gases (WMGHGs) and aerosols for the period 2020–2050 under the three latest Covid-19 economic-recovery scenarios using an aerosol-climate model. The results indicate that reductions in both WMGHG and aerosol emissions under the Covid-19 green recoveries lead to increases ranging from 0 to 0.3 W m^{-2} in global annual mean anthropogenic ERF over the period 2020–2050 relative to the Shared Socioeconomic Pathway 2-4.5 scenario (the baseline case). These positive ERFs are mainly attributed to the rapid and dramatic decreases in atmospheric aerosol content that increase net shortwave radiative flux at the top of atmosphere via weakening the direct aerosol effect and low cloud cover. At the regional scale, reductions in aerosols contribute to positive ERFs throughout the Northern Hemisphere, while the decreased WMGHGs dominate negative ERFs over the areas away from aerosol pollution, such as the Southern Hemisphere oceans. This drives a strong interhemispheric contrast of ERFs. In contrast, the increased anthropogenic emissions under the fossil-fueled recovery scenario lead to an increase of 0.3 W m^{-2} in global annual mean ERF in 2050 compared with the baseline case, primarily due to the contribution of WMGHG ERFs. The regional ERF changes are highly dependent on local cloud radiative effects.

Plain Language Summary As a result of the Covid-19 pandemic, the unprecedented containment has imposed on energy demand and other structural changes in transport globally. These changes may further affect future emission levels, thus inducing climate changes at the global and regional scales. In this study, we estimated effective radiative forcings (ERFs) due to anthropogenic forcing agents, such as well-mixed greenhouse gases (WMGHGs), and aerosols, under the three latest Covid-19 economic recovery scenarios (fossil-fueled, moderate green, and strong green recoveries). Despite large decreases in both WMGHG and aerosol emissions under two green recovery scenarios, we found the aerosol ERF that mainly occurs over the Northern Hemisphere is the dominant contributor to the total positive ERFs over the period 2020–2050. Conversely, the ERFs over the Southern Hemisphere oceans turn negative due to the reduction in WMGHG emissions, which partly offset the effects of the abovementioned changes in aerosols, and result in asymmetric interhemispheric patterns in Earth's radiation budget in future.

Key Points:

- Reductions in aerosol emissions under two green recoveries dominate the increases in total effective radiative forcing (ERF) from 2020 to 2050
- Compared to 2020, the total ERF increases in 2050 due to increased greenhouse gas under a fossil-fueled recovery
- Interhemispheric contrasts of ERF are striking due to the simultaneous decreased anthropogenic forcing agents

Supporting Information:

Supporting Information may be found in the online version of this article.

Correspondence to:

H. Zhang,
huazhang@cma.gov.cn

Citation:

Yu, X., Zhang, H., Xie, B., Wang, Z., Zhao, S., & Zhao, D. (2022). Effective radiative forcings due to anthropogenic emission changes under Covid-19 and post-pandemic recovery scenarios. *Journal of Geophysical Research: Atmospheres*, *127*, e2021JD036251. https://doi.org/10.1029/2021JD036251

Received 23 NOV 2021
Accepted 4 APR 2022

1. Introduction

To date, the damage resulting from the Coronavirus Disease 2019 (Covid-19) pandemic continues globally. There was a sharp drop in anthropogenic emissions in the early stage of the pandemic due to the severe restrictions on travel and economic activities worldwide (Le Quéré et al., 2020; Z. Liu et al., 2020; Zheng et al., 2020). The aftermath of this pandemic has contributed to the decrease in carbon dioxide (CO_2) emissions in 2020 and 2021, both relative to 2019 levels (United Nations Environment Programme, 2021). The impact of Covid-19 on emissions is expected to continue, since the Covid-19-related rescue spending and recovery investment have set out in a low-carbon way in several countries, such as China, Germany, and the United Kingdom (Keramidas et al., 2021;

United Nations Environment Programme, 2020, 2021). Although previous studies have revealed slight effects of reduced emissions associated with Covid-19 containment on the global mean values of radiative forcing, surface air temperature, and precipitation (Fasullo et al., 2021; Gettelman et al., 2020; Weber et al., 2020), but these decreased emissions contributed importantly to the 2020 extreme summer rainfall at the regional scales (Fadnavis et al., 2021; Y. Yang et al., 2022). Moreover, stronger climate responses may emerge if the economic stimulus policies at post-pandemic result in persistent changes in anthropogenic emissions (Forster et al., 2020; Y. Yang et al., 2020; Z. L. Wang et al., 2016).

Emission policies that balance Covid-19 containment and post-pandemic economic recovery may drive future climate changes at the global and regional scales, which becomes a major concern of societies and scientists (Balkan Green Energy News, 2020; European Commission, 2020; Hepburn et al., 2020; Qian et al., 2020). Therefore, a new model intercomparison project that accounts for the effects of Covid-19 (Covid-MIP) has been included within the Coupled Model Intercomparison Project Phase 6 (CMIP6) to assess the potential climate effects of anthropogenic emission changes under Covid-19 pandemic and post-pandemic recovery scenarios (Lamboll et al., 2021). Isolating and comparing effective radiative forcings (ERFs) from individual emission types or categories is encouraged by the protocol for Covid-MIP due to the competing or offsetting effects of these reduced emissions on global and regional climate.

ERF is defined by the change in the net radiative flux at the top of the atmosphere (TOA) following adjustments in both tropospheric and stratospheric temperatures, water vapor, and clouds, but with surface temperature or a portion of surface conditions unchanged (Myhre, Shindell, et al., 2013). The metric that evaluates the contribution of a specific atmospheric component to climate change can only be obtained via the modeling approach, since it is difficult to derive the global tropospheric adjustment terms without using a comprehensive climate model. Previous studies have reported the dominant contributions of well-mixed greenhouse gases (WMGHGs) to global warming over the Industrial Era, with the best estimate of ERF reaching 2.83 (2.26–3.40) W m^{-2} (Myhre, Shindell, et al., 2013; Oshima et al., 2020; Xie et al., 2016). However, aerosols are closely linked to changes in regional radiation budgets and near-term climate changes due to their short lifetimes, complex distributions, and aerosol-cloud interactions (Li et al., 2019; Y. W. Liu et al., 2018). For example, Oshima et al. (2020) indicated that black carbon (BC) was the second-largest contributor to positive ERF over the Arctic, after WMGHGs. The aerosol ERF over eastern China from 1850 to 2005 was estimated to be −4.14 W m^{-2} based on CMIP5 multi-model analysis (R. J. Liu & Liao, 2017). Recent studies have shown that detectable increases in surface radiative fluxes and air temperatures under the Covid-19 pandemic are attributed mainly to reduced aerosol concentrations (Heerwaarden et al., 2021; Peters et al., 2020; Y. Yang et al., 2020), despite sharp drops in both WMGHG and aerosol emissions around the world (Le Quéré et al., 2020; Z. Liu et al., 2020; Lokhandwala & Gautam, 2020; Zheng et al., 2020). Therefore, aerosol forcing contributes to a large uncertainty in the total anthropogenic ERF due to the inhomogeneous spatial patterns of aerosol concentrations, and aerosol-cloud interactions (Grandey et al., 2018; Mulcahy et al., 2018; Ren et al., 2020; H. Wang et al., 2020; Y. Yang, Smith, Wang, Mills, & Rasch, 2019; Zhang et al., 2016). The competing or offsetting effects of aerosols and WMGHGs also make predictions of future climate changes more challenging at the global and regional scales.

The Fifth Assessment Report (AR5) of the Intergovernmental Panel on Climate Change emphasized changes in future emissions of GHGs and aerosol precursors as a second source of uncertainty stems in predicting future climate changes (Cubasch et al., 2013). Using an aerosol-climate coupled model, Zhang et al. (2018) reported the apparent differences among ERFs of short-lived climate pollutants under different Representative Concentration Pathways, with the global mean ERF ranging from −0.5 to 0.1 W m^{-2} base on low-and-high emissions scenarios, respectively. By modifying gridded projections from the Shared Socioeconomic Pathway (SSP) 2–4.5, Forster et al. (2020) and Lamboll et al. (2021) provided four updated projections showing the potential impacts of Covid-19 on future anthropogenic emissions. Fiedler et al. (2021) indicated an aerosol ERF spread of −0.68 to −0.38 W m^{-2} for 2050 under these post-pandemic recovery scenarios. Although the post-pandemic economic recovery scenarios are highly idealized, they provide several possible global emissions trends in the future, which consider the potential impacts of Covid-19 on government investment from countries toward either the fossil fuel economy or green infrastructure (Andrijevic et al., 2020; Gillingham et al., 2020). These idealized Covid-MIP scenarios incorporate the impact of Covid-19 pandemic into projections of socioeconomic development for the 21st century, thereby supplement the projections of greenhouse gas emission pathways of integrated assessment model scenarios, that is, the SSP scenarios. The green recovery scenarios may lend opportunities to further

advance understanding of how climate respond to long-term emission reductions, as a preview for achieving the 1.5°C Paris Agreement goal (Röser et al., 2020; Tolliver et al., 2020), especially for examining the contribution from different anthropogenic forcing agents to global warming. Therefore, transient simulations with forcing agents that evolve over time are employed in this study to estimate the transient contributions of WMGHGs and aerosols to ERFs.

We quantitatively estimate the time evolution of ERFs due to anthropogenic WMGHGs and aerosols for the period 2020–2050 under different Covid-19 recovery scenarios using a global aerosol-climate model of BCC_AGCM2.0_CUACE/Aero (see detail in Section 2.2). The scenarios, model, and methods used in this paper are presented in Section 2. Changes in anthropogenic agents and their combined and individual ERFs under three scenarios are analyzed in Sections 3–5. The discussion and conclusions are presented in Section 6.

2. Methodology

2.1. Covid-19 Recovery Scenarios

Following the protocol for Covid-MIP, the SSP2-4.5 emission scenario is employed as the baseline scenario. This scenario envisions a central pathway without substantial deviations and keeps emissions at low to medium level, which is applicable to inter-decadal and near-term climate predictions (O'Neill et al., 2016; Riahi et al., 2016). The SSP2-4.5 data sets that include WMGHGs (e.g., CO_2, methane [CH_4], and nitrous oxide [N_2O]), aerosols (e.g., BC, organic carbon [OC], and sulphate [SF]), and their precursors (e.g., sulfur dioxide [SO_2]) are downloaded from the input data sets platform for model intercomparsion projects (Feng et al., 2020; Input4MIPs, 2020; https://esgf-node.llnl.gov/search/input4mips/). Note that the WMGHG data sets are concentration data, while the others are emission data.

According to the assumptions that imply the impacts of Covid-19 containment as well as post-pandemic emission policies, three recovery pathways from 2020 to 2050 are employed: a pathway supporting increased fossil-fuel use ("fossil-fueled recovery") and two pathways encouraging moderate or large green stimulus ("moderate green recovery" and "strong green recovery", respectively). These scenarios follow the "two-year-blip" pathway, based on the assumption that 66% of the June 2020 reduction in emissions persists until the end of 2021, after which emissions diverge at the end of 2022 following assumptions corresponding to different economic recoveries (Forster et al., 2020). The fossil-fueled recovery follows a more fossil investment trajectory, which assumes that emissions are 10% higher in 2030 than the baseline scenario and will keep growing in the same trend thereafter. The two green recovery scenarios assume more investment for low-carbon technologies (increases ranging from 0.8% to 1.2% than a pre-Covid-19 current-policy scenario), resulting in about a 35% and a slightly more than 50% decrease of WMGHG emissions by 2030, respectively, compared to the baseline scenario. Continuing these emission assumptions will lead to global net-zero CO_2 by 2060 and 2050, respectively.

Figure 1 shows the time evolution of changes in the concentrations of WMGHGs in the baseline pathway and three Covid-19 economic recovery scenarios relative to 2020. In the baseline pathway scenario, the concentrations of CO_2 and N_2O increase by 7.1% and 1.6% per decade, respectively; but the concentration of CH_4 declines by −1.8% per decade. Although WMGHG emissions increase in the fossil-fueled recovery scenario, these changes exert limited impacts on atmospheric WMGHG concentrations, with increases within 5% for CO_2, CH_4, and N_2O in 2050 compared to the baseline pathway. However, under the two green recovery scenarios there are apparent reductions in WMGHG concentrations relative to the baseline pathway, with declines of 11.5% (15.2%), 15.9% (26.4%), and 1.3% (3%) for CO_2, CH_4, and N_2O, respectively, in 2050 under the moderate (strong) green recovery scenario. In general, the impacts of changes in WMGHG emissions on their atmospheric contents are more pronounced after 2030 for all Covid-19 economic recovery scenarios. Note that the time evolution of changes in aerosol emissions under the three Covid-19 economic recovery scenarios compared to the baseline case is consistent with those of WMGHG concentrations. Changes in the aerosol concentrations under these scenarios are analyzed in Section 3.

2.2. Model and Experiments

We use the global aerosol-climate model of BCC_AGCM2.0_CUACE/Aero developed by Z. L. Wang et al. (2014), Zhang et al. (2014), and Zhang, Wang, et al. (2012). This model incorporates a range of revisions that allow it

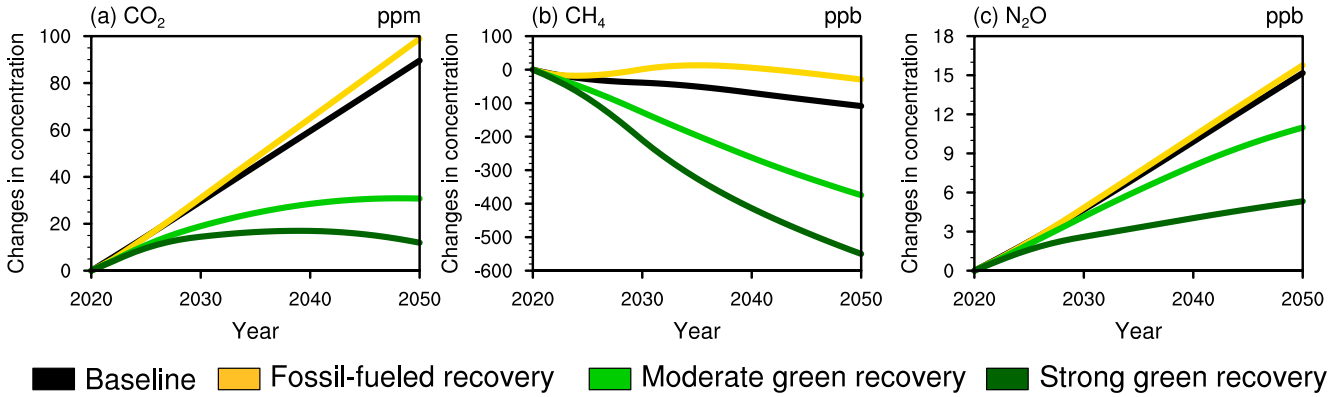

Figure 1. Time evolution of changes in the global annual mean concentrations of (a) CO_2 (unit: ppm), (b) CH_4, and (c) N_2O (units: ppb) in the baseline pathway and three Covid-19 economic recovery scenarios relative to 2020. The black, gold, green, and dark green lines represent the baseline pathway, fossil-fueled, moderate green, and strong green recovery scenarios, respectively.

to evaluate ERF well. Its atmospheric component, named as the Atmospheric General Circulation Model of the Beijing Climate Center version 2.0 (BCC_AGCM2.0), was developed by the Beijing Climate Center of Chinese Meteorological Administration (CMA; Wu et al., 2010), which employs a horizontal T42 spectral resolution (approximately 2.8° × 2.8°) and a terrain-following hybrid vertical coordinate, with 26 layers and a rigid lid at 2.9 hPa. The radiation scheme BCC_RAD and the Monte Carlo independent column approximation (McICA) cloud vertical overlap scheme (Jing et al., 2016; Zhang et al., 2014) were introduced in BCC_AGCM2.0. The optical properties of water and ice clouds were taken from Nakajima et al. (2000) and Zhang et al. (2015), respectively. These schemes reduce error in the simulated TOA longwave and shortwave radiative fluxes.

Five aerosol species, including BC, OC, SF, dust (SD), and sea salt (SS) are contained in the CUACE/Aero aerosol model (CMA Unified Atmospheric Chemistry Environment for Aerosols), which was developed by the Chinese Academy of Meteorological Sciences. CAUCE/Aero considers aerosol emissions, transport, chemical conversion, interactions with cloud and sedimentation processes (C. H. Zhou et al., 2012). Emissions of BC, OC, SF, and their precursors are prescribed, while natural emissions of SD and SS are calculated online (Alfaro & Gomes, 2001; Gong et al., 2003, 2002; Marticorena & Bergametti, 1995). Each type of aerosol is divided into 12 consecutive non-overlapping bins as a geometric series for radii between 0.005 and 20.48 μm to ensure a precise characterization of the concentrations and optical properties of aerosols with various particle sizes in the model. Aerosol optical properties are given by Wei and Zhang (2011) and Zhang, Shen, Wei, Zhang, & Li (2012). BCC_AGCM2.0_CUACE/Aero adopts a two-moment cloud microphysical scheme (Gettelman et al., 2008; Morrison & Gettelman, 2008) to describe the cloud microphysical and aerosol-cloud interaction processes (Z. L. Wang et al., 2014). This allows physical representations of aerosol direct, semi-direct, and indirect effects for liquid-phase clouds, and ensures more reliable simulations of aerosol ERFs from BCC_AGCM2.0_CUACE/Aero than those from other models with one-moment schemes (Grandey et al., 2018; H. Wang et al., 2020).

The model has shown reasonable performance in simulating meteorological field and aerosols by participating international comparisons, such as CMIP5 (T. J. Zhou, Chen, 2014; T. J. Zhou, Zou, et al., 2014), and the AeroCom Phase II (Myhre, Myhre, et al., 2013; Tsigaridis et al., 2014). It has been widely used in quantifying ERFs related to aerosol-radiation interactions (ERFari), and aerosol-cloud interactions (ERFaci; Zhang et al., 2018; 2016; C. Zhou et al., 2017).

Four groups of experiments, referred to hereinafter as Exp_Ref, Exp_All, Exp_Aero, and Exp_GHG, are performed to assess the combined ERFs of both WMGHGs and aerosols, as well as the individual ERFs of these forcing agents (Table 1). Each group of experiments uses the same model settings, but with different forcing pathways. Four experiments are performed in the Exp_All group as shown in Table 1 too. By changing the initial atmospheric conditions, each experiment includes five members to minimize disturbances related to model-internal variability (Lamboll et al., 2021). The first experiment is driven by the SSP2-4.5 forcing (Exp_All_ssp2-4.5). The other three experiments are driven by different Covid-19 economic recovery pathways, that is, fossil-fueled recovery (Exp_All_FFR), moderate green recovery (Exp_All_MGR), and strong green recovery (Exp_All_SGR) experiments. Notably, these experiments are simultaneously forced by both WMGHG concentration and aerosol

Table 1
Experimental Design

Group	Experiment	Period	Experiment description	Sea temperature
Exp_All	Exp_All_ssp2-4.5	2020–2050	Time-varying anthropogenic forcings, including the WMGHGs and aerosols, under the SSP2-4.5 pathway	Prescribed SST
	Exp_All_FFR		Time-varying anthropogenic forcing, including the WMGHGs and aerosols, under fossil-fueled, moderate green, and strong green recovery scenarios	
	Exp_All_MGR			
	Exp_All_SGR			
Exp_Aero	Exp_Aero_FFR		Time-varying aerosol forcing under fossil-fueled, moderate green, and strong green recovery scenarios	
	Exp_Aero_MGR			
	Exp_Aero_SGR			
Exp_GHG	Exp_GHG_FFR		Time-varying WMGHGs forcing under fossil-fueled, moderate green, and strong green recovery scenarios	
	Exp_GHG_MGR			
	Exp_GHG_SGR			

Group	Experiment	Running time	Pathway	Year	Sea temperature
Exp_Ref	Exp_Ref_ssp2-4.5	12	SSP2-4.5	2020	Prescribed SST

emission data. Both Exp_Aero and Exp_GHG groups consist of three Covid-19 recovery scenario experiments that kept the same model settings as the Exp_All group, except using aerosol emissions and WMGHG concentrations, respectively. Each simulation is transient and driven by forcing agents evolving from 2020 to 2050. A time-slice simulation (i.e., a reference experiment, Exp_Ref_ssp2-4.5 for short) is carried out in the Exp_Ref group. This experiment is run for 12 yr by employing the SSP2-4.5 pathway that is fixed at 2020, and the average results of the last 10 yr are analyzed.

2.3. Methodology for ERF Calculations

All groups in this study adopt the method of fixed sea surface temperatures (SSTs), that is, the fixed-SST (fSST) method defined by AR5, for ERF calculations. This approach shows consistently smaller uncertainty than regression-based method since it avoids biases derived from nonlinearity in the relationship between TOA irradiance and surface temperature change in the coupled simulations (Forster et al., 2016). Another advantage of the fSST method is that it consistently separates forcing and feedback regardless the length of integration, and thus can be used to estimate transient ERF from a scenario with time-varying forcing agents. More importantly, previous studies have indicated that ERF is weakly dependent on background state, which means that choosing any annually repeating monthly averaged SST and sea ice climatology is feasible (Forster et al., 2016; Pincus et al., 2016). Therefore, the climatological monthly mean SST and sea ice data from 1981 to 2010 are specified as the oceanic boundary conditions in this study.

It is noted that the change in near-surface temperature over land, that is, ΔT_{land}, is not constrained in the fSST method, and this response should be removed for consistency with the definition of ERF (Tang et al., 2019). This correction on ERF can be approximately addressed by subtracting the radiative response to ΔT_{land} from the initial ERF based on the fSST method (ΔF_{fsst}). The formula is as follows:

$$\text{ERF} \approx \Delta F_{\text{fsst}} - k * \Delta T_{\text{land}} \quad (1)$$

where k is a precomputed kernel that represents the change in net TOA radiative flux per change in unit near-surface temperature change over land (Smith et al., 2020). The above correction approach described in Tang et al. (2019) is employed in our ERF estimation under the Covid-19 recovery scenarios. Moreover, we choose to quantify transient ERFs with forcing magnitudes of order 0.1 W m^{-2} since diagnosing ERFs of 0.01 W m^{-2} would require centuries of integration (Forster et al., 2016).

Therefore, transient ERFs are computed by differencing net radiative fluxes at the TOA from transient simulations with that from the reference experiment (Pincus et al., 2016). The differences in ERFs under the three Covid-19

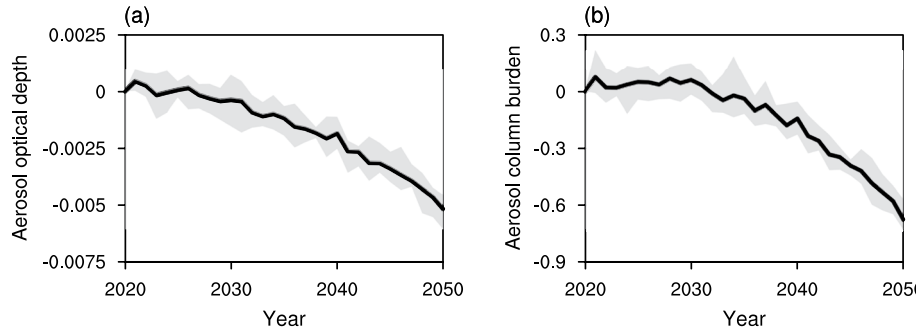

Figure 2. Time evolution of changes in the global annual mean anthropogenic (a) aerosol optical depths (unitless) and (b) aerosol column burdens (unit: mg m^{-2}) under the baseline scenario relative to 2020. The paler plume shows the spread of five ensemble members, whereas the solid line represents their average results.

recovery scenarios compared with the baseline case are defined here as the impacts of different post-pandemic emission policies. The regional features of these differences in ERF during the period of 2020–2050 are estimated by subtracting the 2020–2024 mean from the 2046–2050 mean. This approach helps to reduce the internal noise.

2.4. ERF Sensitivity to Anthropogenic Forcing Agents by the Model of BCC_ AGCM2.0_CUACE/Aero

We assess the transient ERFs from BCC_AGCM2.0_CUACE/Aero using historical multimodel ensemble simulations with all forcing from the Radiative Forcing Model Intercomparison Project (RFMIP) endorsed by CMIP6 (RFMIP-ERF-HistAll; Table S1 in Supporting Information S1). This project aims to diagnose the total time-evolving ERF of both anthropogenic and natural forcing agents under the SSP2-4.5 scenario (Pincus et al., 2016). Figures S1 and S2 in Supporting Information S1 display comparisons between the simulations from BCC_AGCM2.0_CUACE/Aero and the multi-model ensemble results from RFMIP-ERF-HistAll. Our results show comparable spatial distributions and temporal trends to the multi-model mean results. However, our results underestimate the net radiation fluxes at both the TOA and the surface over the Equator and the Tibetan Plateau (TP; Figure S1 in Supporting Information S1). There are slight differences in ERFs and surface radiation fluxes for certain years between our results and the multi-model mean results (Figure S2 in Supporting Information S1). Note that our results exclude the effects of natural forcing agents such as volcanoes, and solar variability. This may have increased the deviations in radiative forcing in special years between our results and the RFMIP-ERF-HistAll simulations (Myhre, Shindell, et al., 2013; Pincus et al., 2016).

3. Changes in Aerosol Concentrations and Optical Depth

Figure 2 displays the time evolution of changes in global annual mean anthropogenic aerosol optical depths (AAODs) and aerosol column burdens (AACBs) under the baseline scenario relative to 2020. In this study, anthropogenic aerosols comprise BC, OC, and SF, the atmospheric contents of which are dominated mainly by human activities. Similar to Fiedler et al. (2019) and Lund et al. (2019), there are slight declines of −5.4% and −3.9% per decade in global annual mean AAODs and AACBs, respectively, for the period 2020–2050 under the baseline scenario.

Based on the assumptions of Forster et al. (2020), the impacts of the Covid-19 pandemic on human activities, especially on traffic and the economy, are expected to persist until the end of 2021. The data show reductions in global annual mean AAODs and AACBs until 2022 under all scenarios relative to the baseline case, but subsequent partial recovery by the end of 2022 (Figure 3). After 2023, the time evolution of atmospheric aerosol contents clearly differs among the three Covid-19 economic-recovery scenarios. Under the moderate and strong green recovery scenarios, there are robust decreases in global annual mean AACBs relative to the baseline case (Figure 3b). In the Exp_All group, these decreases are −2.0 and −2.7 mg m^{-2} in 2050, respectively. There are sharp declines in aerosol concentrations until 2030, followed by a slow reduction (Figure 3b). The declining trends reach −0.06 and −0.08 mg m^{-2} yr^{-1} from 2023 to 2050, respectively. Similarly, the global annual mean AAOD values decrease under the moderate and strong green recoveries, with reductions of −0.01 and −0.015 in 2050, respectively, in the Exp_All group (Figure 3a). In contrast, the changes in atmospheric aerosol contents

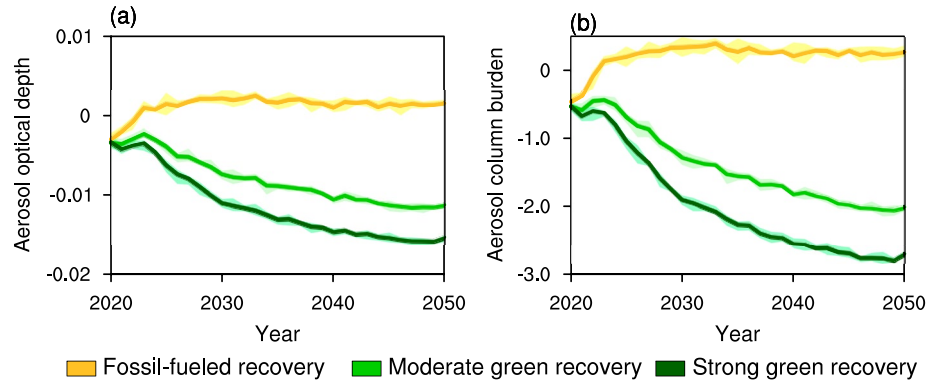

Figure 3. Time evolution of changes in the global annual mean anthropogenic (a) aerosol optical depths (unitless) and (b) aerosol column burdens (unit: mg m^{-2}) under the three Covid-19 economic recovery scenarios relative to the baseline case in the Exp_All group. The gold, green, and dark green lines represent fossil-fueled, moderate green, and strong green recovery scenarios, respectively. The paler plumes show the spread of five ensemble members, whereas the solid lines represent their average results.

are less under a fossil-fueled recovery, with a slight increase of 0.27 mg m^{-2} in the global annual mean AACBs in 2050 in the Exp_All group. In addition, the increase in global annual mean AAODs is less than 0.002. There is an uptrend of 0.04 mg m^{-2} yr^{-1} in the global annual mean AACBs until 2030. Thereafter, this increasing trend weakens, and is characterized by inter-annual fluctuations. These slight increases in atmospheric aerosol contents, especially for AAODs, are attributed mainly to smaller emission growth (increase by 10% in 2030) with a fossil-fueled recovery.

As seen in Figure 4a (Figure 5a), there are general decreases in annual mean AACBs (AAODs) over the Northern Hemisphere (NH), while the atmospheric aerosol contents increase over southern central Africa. These changes in aerosols at the regional scale are mainly attributed to emissions in SSP2-4.5 that follows an intermediate pathway—a global decline throughout the century with regional variations due to different energy system structures (Fricko et al., 2016). Similar changes in AACBs and AAODs can be seen in previous findings (Fiedler et al., 2019; Lund et al., 2019). Compared to the baseline case, there are sharp declines in AACBs worldwide under the two green recovery scenarios, especially over the NH middle and low latitudes, as well as on both sides of the equatorial Africa. The maximum decreases exceed 10 mg m^{-2} over eastern China, the Indian Peninsula, and the south side of equatorial Africa (Figures 4c and 4d). Similarly, there are obvious decreases in AAODs over the NH continents and Africa, with maximum changes exceeding 0.1 over eastern China (Figure 5d). The increases in AACBs under a fossil-fueled recovery are concentrated mainly in regions with intensive human activities and the adjacent oceans, such as the eastern coasts of Eurasia, the Indian Peninsula, central Asia, and central and southern Africa, where the maximum increases exceed 1 mg m^{-2} (Figure 4b). The geographical distributions of changes in AAODs are negligible under this scenario. The positive anomalies of AAODs are mainly located along the eastern coasts of Eurasia and northern Pacific (Figure 5b).

4. Changes in ERFs

Figure 6 shows transient ERFs contributed by anthropogenic forcing agents under the baseline scenario and three Covid-19 recovery scenarios relative to 2020. Figures 6b and 6c indicate the attributable ERFs from aerosols and WMGHGs, respectively. The combined ERF of anthropogenic WMGHGs and aerosols for the period 2020–2050 under the baseline scenario is 1.1 (0.7–1.5) W m^{-2}. Under the moderate and strong green recovery scenarios, the significant decreases in atmospheric aerosol contents result in an increase in ERFs over the period by 0.8 and 1 W m^{-2} relative to the baseline case for 2020–2050, respectively (Figure 6b and Table 2). Compared to the changes in aerosols, these green stimuli exert little impact on near-term WMGHG contents in the air due to the longer lifetimes of WMGHGs (Figure 1). However, there is an apparent division in transient ERF between the scenarios after 2030 (Figure 6c), with decreases of −0.6 and −0.8 W m^{-2} in ERFs contributed by declining WMGHG emissions relative to the baseline case for the period 2020-2050, respectively (Table 2); overall, the decrease in anthropogenic WMGHG and aerosol emissions leads to changes of 0 and 0.3 W m^{-2} in the combined ERFs relative to

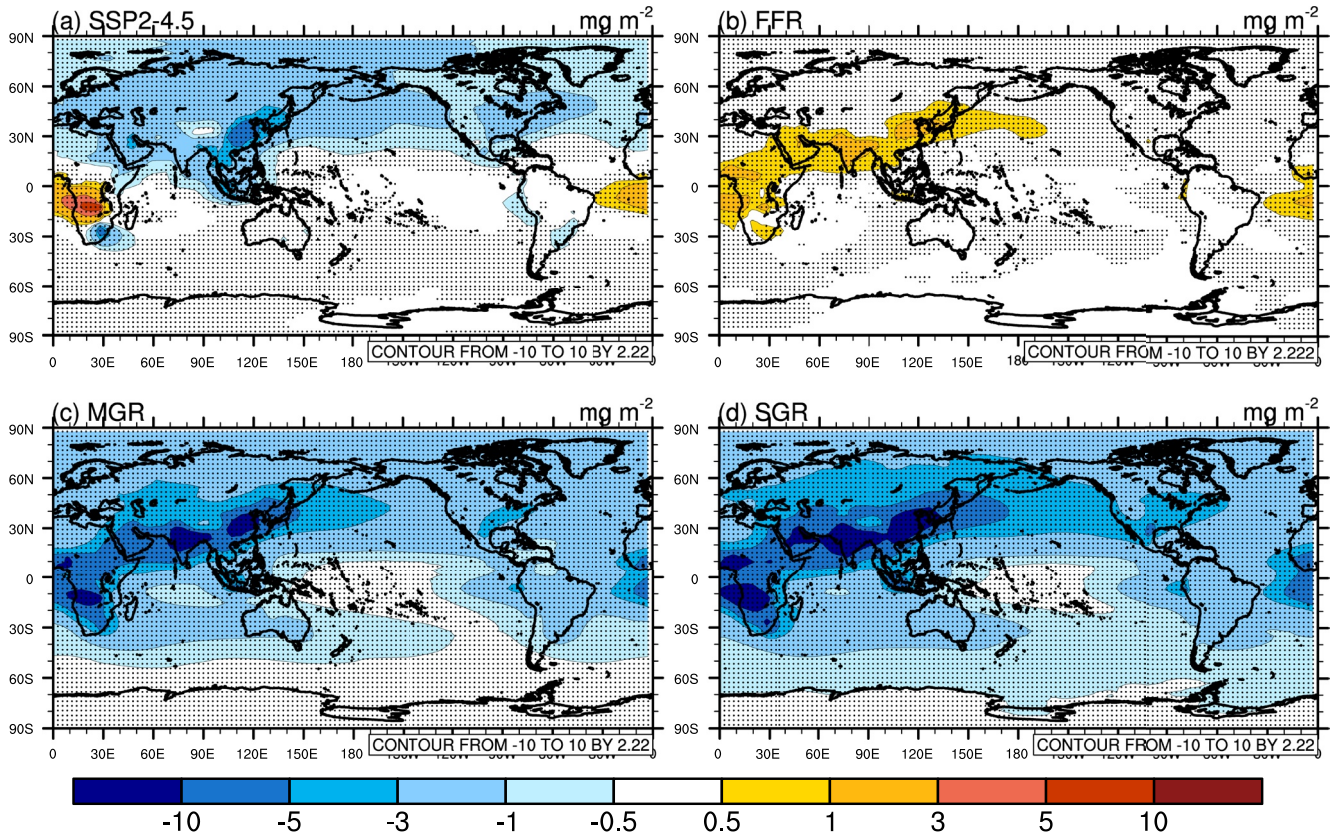

Figure 4. (a) Changes in annual mean anthropogenic aerosol column burdens (unit: mg m^{-2}) during the period of 2020–2050 for the baseline case; (b–d) changes in annual mean anthropogenic aerosol column burdens (unit: mg m^{-2}) under fossil-fueled, moderate green, and strong green recovery scenarios relative to the baseline case for the period 2020–2050. The dots indicate significance at the ≥90% confidence level from a *t* test.

the baseline case, respectively, which are smaller in magnitude than the individual contributions to ERF changes. These changes in ERFs are primarily attributed to declining atmospheric aerosol contents, especially before 2035 (Figures 3, 7a, and 7b). This rapid weakening of negative aerosol forcing is expected to exacerbate the global warming driven by WMGHGs by the mid-21st century (Lund et al., 2019; Westervelt et al., 2015). However, the impacts of reduced WMGHG emissions on the Earth's radiation budget emerge after 2030, due to the sharper decrease in WMGHG concentrations (Figures 1, 6c, and 7c). This partly offsets the above effects of aerosols (Figures 6a and 7a). Under a fossil-fueled recovery, the combined ERF due to WMGHGs and aerosols for 2050 is 1.4 (0.9–1.9) W m^{-2}, with an increase of 0.3 W m^{-2} in ERF relative to the baseline case (Figure 6a and Table 2). This increased ERF is attributed mainly to the persistent increase in WMGHG, especially after 2045 (Figure 7c). In addition, increased aerosol emissions generally contribute to a decrease in ERFs after 2025 (Figure 7b).

Figure 8 (left panel) shows the geographical distributions of changes in the annual mean combined ERFs from both WMGHGs and aerosols over the period 2020–2050 under three Covid-19 recovery scenarios relative to the baseline case. The responses of the radiation budget to anthropogenic emissions are stronger at the regional scale, although the magnitudes of the global mean responses remain small.

As seen in Figure S3a in Supporting Information S1, anthropogenic WMGHG and aerosol emissions under the baseline pathway lead to generally positive ERFs worldwide for the period 2020–2050. Compared to the baseline case, there are significant increases in ERFs over the NH continents and their adjacent oceans, as well as in the south of equatorial Africa under the two green recovery scenarios, with maximum increases exceeding 5 W m^{-2} (Figures 8d and 8g). For the strong green recovery scenario, decreased anthropogenic emissions contribute to significant increases in ERFs over almost all of the NH continents and the North Pacific, with the exception of northwestern India and North Africa (Figure 8g). These increases in ERFs are primarily attributed to sharp reductions in atmospheric aerosol contents over the areas with intensive human activities, weakening the scattering

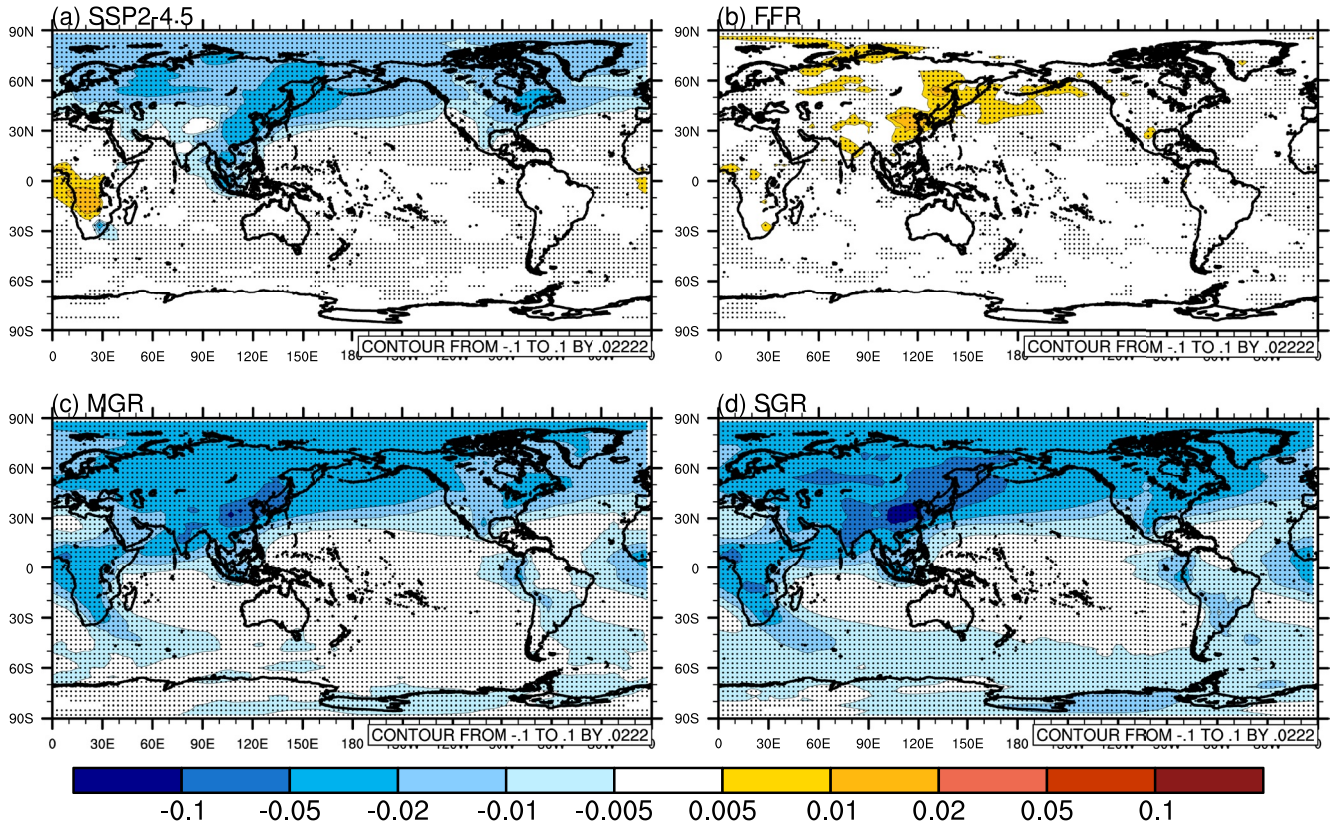

Figure 5. Same as Figure 4, but for changes in annual mean anthropogenic aerosol optical depths (AAODs).

effects of aerosols on shortwave radiation (Figure S4c in Supporting Information S1; D. D. Yang, Zhang, & Li, 2019). However, decreased aerosol contents in the air lead to reductions in ERFs over North Africa, northwest India, and central parts of North America as a result of enhanced reflection of solar radiation over these high-albedo areas (Myhre, Samset, & Storelvmo, 2013).

Moreover, the rapid adjustment of clouds induced by changes in anthropogenic emissions plays an important role in modifying the Earth's radiation budget (Smith et al., 2020, 2018). Under the two green recovery scenarios, there are significant decreases in low-cloud cover over northern and southeastern Pacific, as well as northeastern Atlantic (Figures 9b and 9c), leading to more solar radiation reaching these places. Conversely, low-cloud

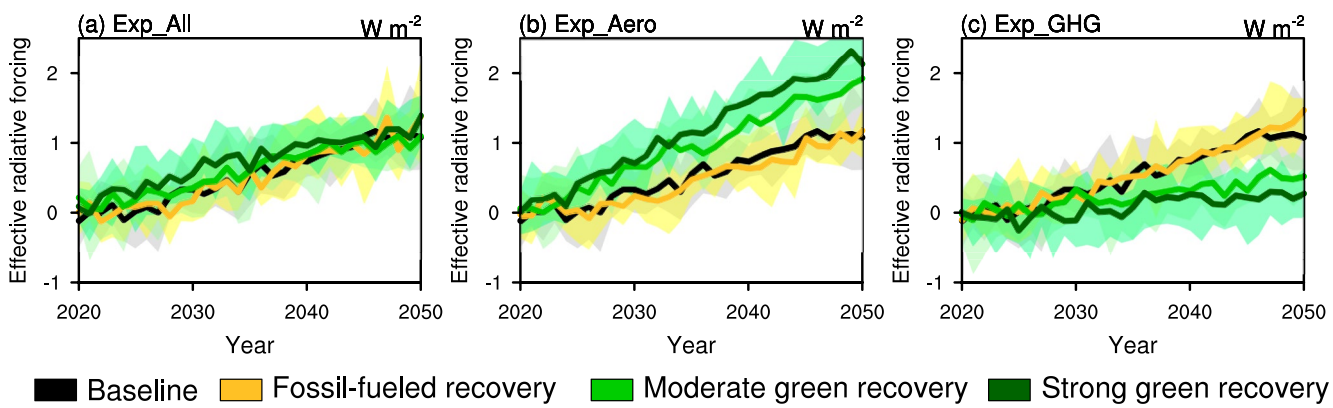

Figure 6. Transient effective radiative forcings (ERFs; unit: W m^{-2}) under the baseline scenario and three Covid-19 economic recovery scenarios, relative to 2020, in the (a) Exp_All, (b) Exp_Aero, and (c) Exp_GHG group. The black, gold, green, and dark green lines represent the baseline scenario, fossil-fueled, moderate green, and strong green recovery scenarios, respectively. The paler plumes show the spread of five ensemble members, whereas the solid lines represent their average results.

Table 2
ERFs (unit: W m^{-2}) for 2050 Under the Baseline Scenario and Three Covid-19 Economic Recovery Scenarios in the Exp_All, Exp_Aero, and Exp_GHG Group

	Exp_All	Exp_Aero	Exp_GHG
Baseline	1.1 (0.7–1.5)		
Fossil-fueled recovery	1.4 (0.9–1.9)	1.2 (0.9–1.4)	1.5 (1.3–1.7)
Moderate green recovery	1.1 (0.8–1.4)	1.9 (1.7–2.1)	0.5 (0.3–0.7)
Strong green recovery	1.4 (1.1–1.6)	2.1 (1.8–2.4)	0.3 (0–0.5)

Note. The values in parentheses represent the 5%–95% confidence range.

cover apparently increases over the Southern Ocean and western Indian Ocean, whereby scattering more shortwave radiation at the TOA (Figures 9b and 9c). High-cloud cover significant decreases over eastern Pacific north of the equator, contributing to increases in the outgoing longwave radiation at the TOA here (Figures 10b and 10c). These changes in cloud cover are major contributors to the corresponding ERF changes over the above areas. In addition, there are striking increases in low-cloud cover over southeastern China under the two green recovery scenarios, contributing to negative ERFs over here (Figures 9b and 9c; Figures S6d and S6g in Supporting Information S1). These negative ERFs induced by cloud radiative effects partially offset the positive ERFs caused by direct aerosol effect, resulting in only slight changes in ERF over east coast of the Eurasia under the moderate green recovery scenario (Figure 9d; Figures S5d and S6d in Supporting Information S1), and over southeastern China under the strong green recovery scenario (Figure 9g; Figures S5g and S6g in Supporting Information S1). Similar offset effects are also apparent over central Asia and parts of the West Europe under the moderate green recovery scenario (Figure 9d; Figures S5d and S6d in Supporting Information S1), and over northeastern Eurasia under the strong green recovery scenario (Figure 9g; Figures S5g and S6g in Supporting Information S1). The abovementioned cloud radiative effects only dominate the changes in ERF at the regional scale, especially in the areas away from aerosol pollution, since clouds cover small spatial scale (usually less than several tens km) and keep a shorter lifetime (Oshima et al., 2020; H. Wang et al., 2020).

Under the fossil-fueled recovery scenario, ERFs vary mainly at a local scale (Figure 8a), and are mainly attributed to adjustments in low-cloud cover that dominate the shortwave radiation budgets at the TOA (Figure 9a; Figures S4a and S6a in Supporting Information S1). For example, there are significant decreases in low-cloud cover over the northeast coasts of Eurasia, northwestern and southern Pacific, as well as northeastern Atlantic, which lead to positive ERFs over these areas. Conversely, low-cloud cover shows striking increases over the west of Lake Baikal, contributing to negative ERFs over there.

5. Contributions of WMGHGs and Aerosols to ERFs

Figure 8 (middle and right panels) shows the geographical distributions of changes in the annual mean individual ERFs from aerosols and WMGHGs. The reduced WMGHG emissions induce a decrease in ERFs worldwide under the two green recovery scenarios (Figures 8f and 8i), which is the opposite to the case of anthropogenic aerosols (Figures 8e and 8h). There are apparent differences in the zonal mean changes in ERFs from the WMGHGs and aerosols over the middle latitudes of the NH and SH, and the low latitudes of the SH, where there are three aerosol ERF peaks (Figures 11b and 11c). The decreased aerosol contents lead to significant increases in ERFs over the NH continents and their adjacent oceans, as well as in southern equatorial Africa as a result

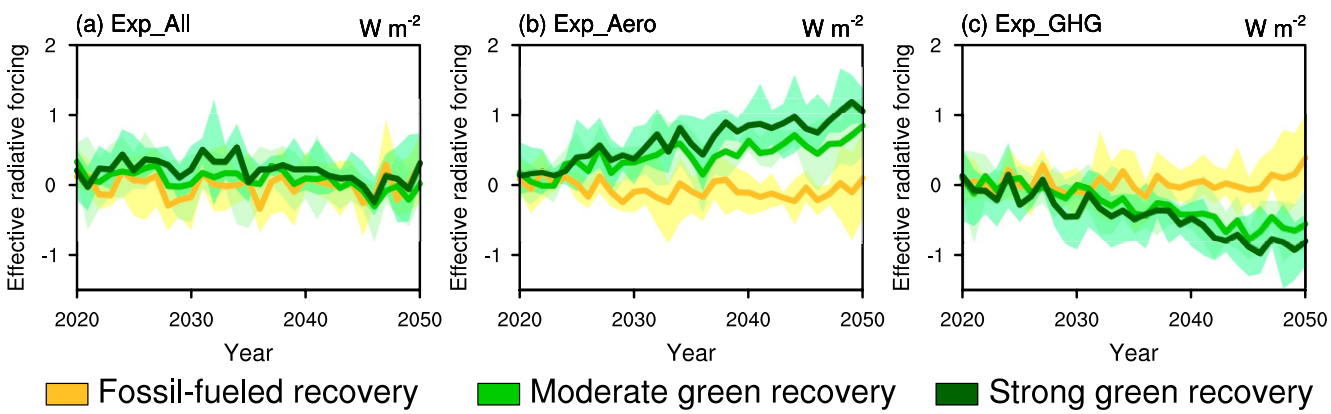

Figure 7. Time evolution of changes in the global annual mean effective radiative forcing (ERF; unit: W m^{-2}) under the three Covid-19 economic recovery scenarios, relative to the baseline case, in the (a) Exp_All, (b) Exp_Aero, and (c) Exp_GHG group. The gold, green, and dark green lines represent fossil-fueled, moderate green, and strong green recovery scenarios, respectively. The paler plumes show the spread of five ensemble members, whereas the solid lines represent their average results.

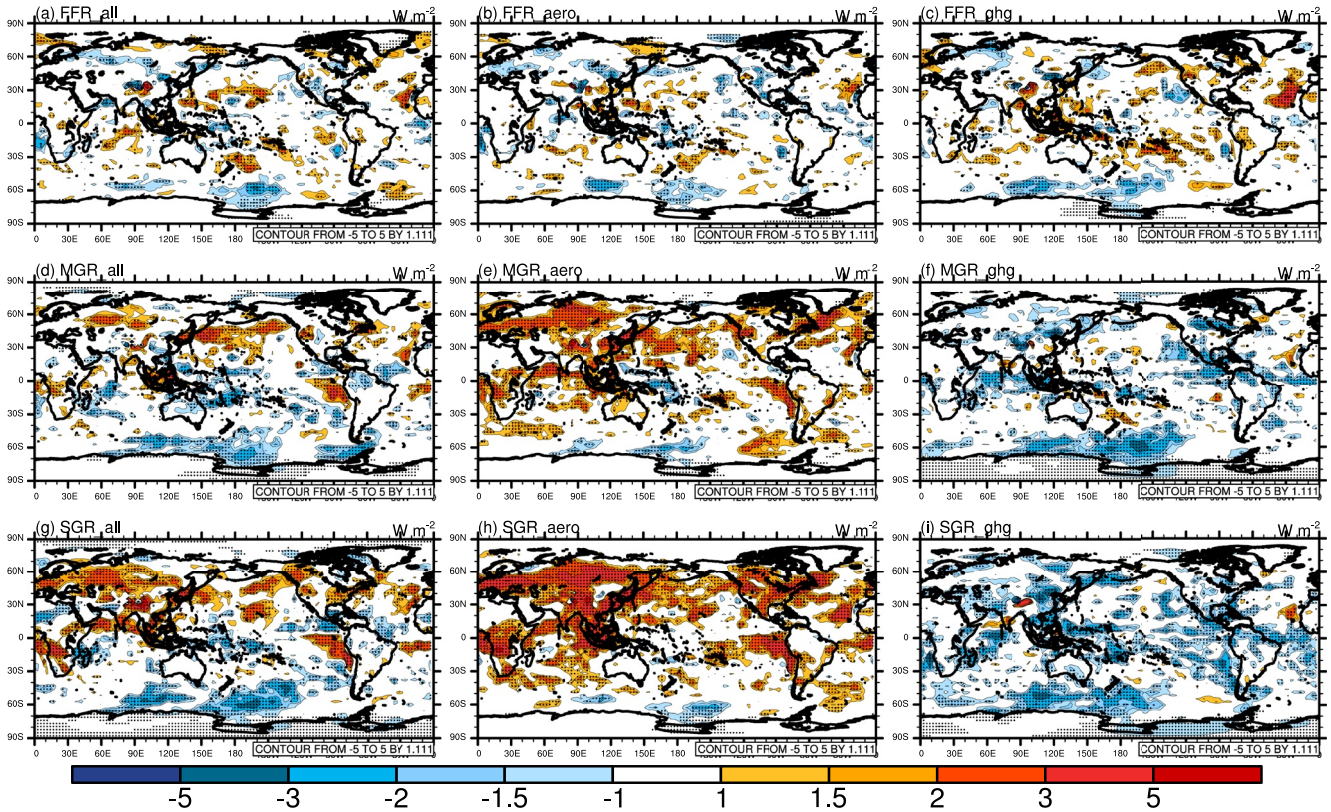

Figure 8. Changes in the annual mean effective radiative forcings (ERFs; unit: W m^{-2}) over the period 2020–2050 under three Covid-19 economic recovery scenarios, relative to the baseline case, in the Exp_All (a, d, g), Exp_Aero (b, e, h), and Exp_GHG (c, f, i) group. The dots indicate significance at the ≥90% confidence level from a *t* test.

of weakening solar radiation reflection (Figures S5e and S5h in Supporting Information S1) and the associated cloud radiative effect (Figures S6e and S6h in Supporting Information S1). Ultimately, this contributes the most to the magnitude of increases in the combined ERFs over the middle latitudes of the NH (Figure 11c). Conversely, the reduced WMGHGs lead to an apparent decrease in ERFs over the oceans in the SH (Figures 8f and 8i; Figures S5f and S5i in Supporting Information S1), mainly contributing to reductions in the combined ERFs over the middle and high latitudes of the SH, especially under the strong green recovery scenario (Figure 11c). The composite effect of reductions in WMGHG and aerosol emissions under the two green recovery scenarios leads to stronger positive anthropogenic ERFs over the NH, but weakly negative anthropogenic ERFs over parts of the SH oceans (Figures S3c and S3d in Supporting Information S1). This composite effect also results in an increase in interhemispheric contrast of ERF by 0.5 (0.2–0.8) and 0.8 (0.7–0.9) W m^{-2}, respectively, compared to the baseline case, larger than that induced by the individual forcing (Table 3). This could further disturb the hemispheric energy balance, the latitudinal location of the intertropical convergence zone, and global and tropical precipitation, via slow oceanic processes and air-sea interactions (Broccoli et al., 2006; Chiang & Bitz, 2005; Schneider et al., 2014; S. Y. Zhao & Suzuki, 2019).

Under the fossil-fueled recovery scenario, ERF changes occur at the regional scale; specifically, a decrease in ERFs due to aerosols occurs near the Lake Baikal and over southwestern North America, whereas an increase in ERFs due to WMGHGs appears over southwestern China, parts of North America, and southern Pacific (Figures 8b and 8c). The ERF changes caused by greenhouse or direct aerosol effects are smaller than those under the two green recovery scenarios (Figures S5b and S5c in Supporting Information S1). This is attributed to the limited increases in anthropogenic emissions (Forster et al., 2020; Lamboll et al., 2021), which induce concentration changes only in their major source areas (Figure 4b). However, these anthropogenic emission changes exert apparent impacts on ERFs as a result of associated cloud cover changes (Figures S6b and S6c in Supporting Information S1). This cloud radiative effect dominates the combined ERF changes over most of the world (Figure S6a in Supporting Information S1). Changes in zonal mean ERFs are messy in latitude by near-zero

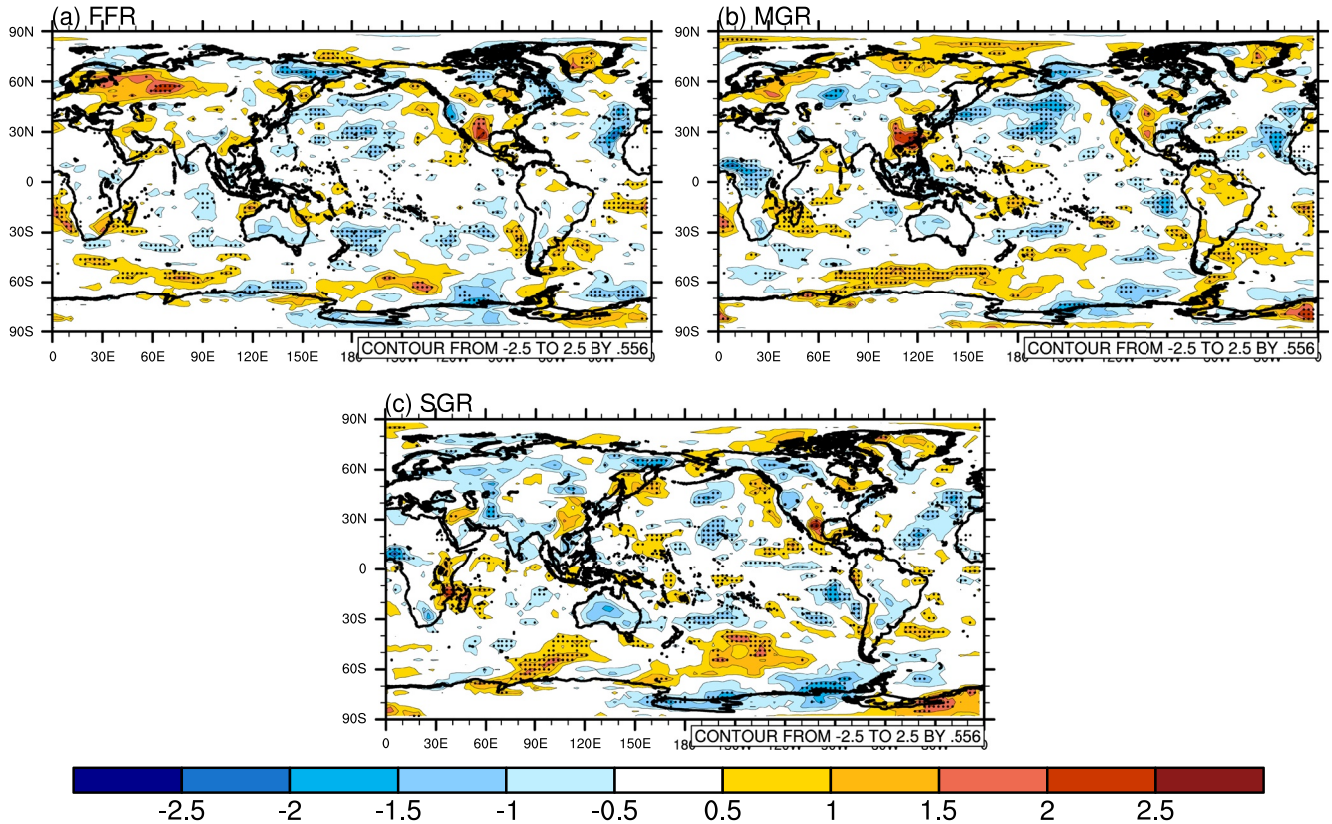

Figure 9. Changes in the annual mean low-cloud cover (unit: 10^{-2} fraction) over the period 2020–2050 under three Covid-19 economic recovery scenarios, relative to the baseline case. The dots indicate significance at the ≥90% confidence level from a *t* test.

fluctuations in all experiment groups (Figure 11a), leading to negligible changes in interhemispheric contrast of ERF, compared to the baseline case (Table 3). This is attributed to the offset between the local positive and negative cloud radiative effects (Figures S6a–S6c in Supporting Information S1). The above analyses indicate that increased anthropogenic emissions contribute to ERF changes only at the regional scale, as opposed to furthering hemispheric differences in ERF.

6. Discussion and Conclusions

This study quantitatively estimates the combined and individual ERFs of WMGHGs and aerosols in response to transient concentration changes under the three Covid-19 recovery scenarios, using an aerosol-climate model of BCC_AGCM2.0_CUACE/Aero, as summarized in following.

There are general decreases in AAODs and AACBs over the NH for the period 2020–2050 under the baseline scenario, similar to the results in Fiedler et al. (2019) and Lund et al. (2019). After 2023, the atmospheric aerosol contents under the two green recovery scenarios further decrease relative to the baseline pathway, consistent with Fiedler et al. (2021). The decreases in AACBs and AAODs are mainly in areas with intense human activities, such as the NH continents and their adjacent oceans, with the maximum annual declines exceeding 10 mg m^{-2} and 0.1, respectively. Due to the smaller emission growth such changes are smaller in magnitude under a fossil-fueled recovery than under the two green recovery scenarios. The increases in atmospheric aerosol contents are concentrated mainly in areas with high anthropogenic emissions such as East Asia, South Asia, and Africa.

Transient ERF due to anthropogenic WMGHG and aerosol emissions over the period 2020–2050 is 1.1 (0.9–1.9) W m^{-2} under the baseline scenario, falling within the ERF spread of RFMIP-ERF-HistAll simulations. Such ERFs are 1.4 (0.9–1.9), 1.1 (0.8–1.4), and 1.4 (1.1–1.6) W m^{-2} under the fossil-fueled, moderate green, and strong green recovery scenarios, respectively. These increases in ERFs under the three Covid-19 economic-recovery scenarios not only imply further global warming by the mid-21st century (Lewinschal et al., 2019;

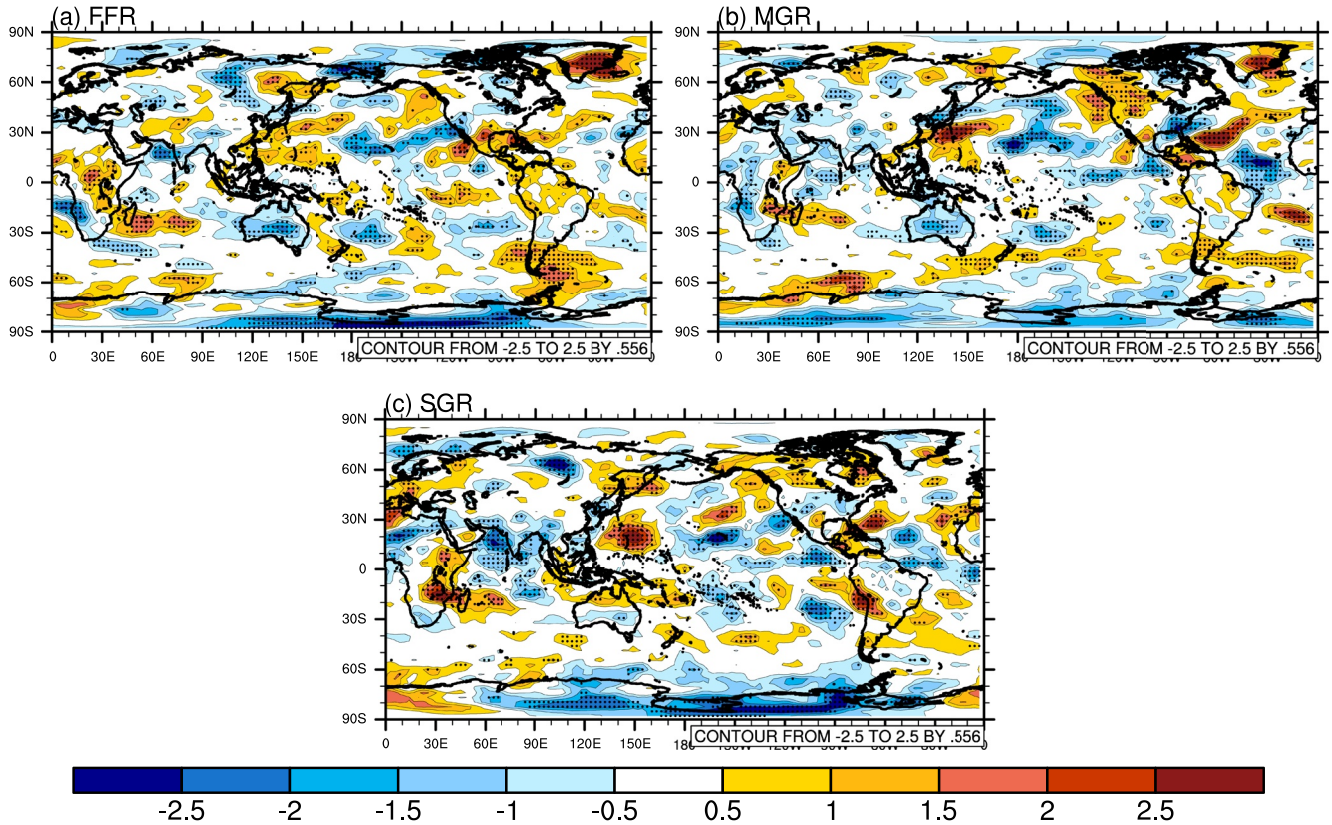

Figure 10. Same as Figure 9, but for changes in high-cloud cover (unit: 10^{-2} fraction).

Westervelt et al., 2015; D. D. Yang, Zhang, et al., 2019) but also indicate the complexity of the combined effects of varying WMGHG and aerosol emissions on future climate change under different scenarios (Myhre, Shindell, et al., 2013; Oshima et al., 2020; A. Zhao et al., 2019). Under moderate and strong green recoveries, the decrease in aerosol emissions leads to increases of 0.8 and 1.0 W m^{-2}, respectively, in the global annual mean ERF relative to the baseline case. A previous study expected anthropogenic warming to be the weakest in the strong green recovery scenario, due to a larger reduction in WMGHG emissions (Fiedler et al., 2021). However, our results emphasize the dominant role of anthropogenic aerosols in driving climate change through the first half of the 21st century. The decrease in WMGHG emissions contributes to reductions in ERF of −0.6 and −0.8 W m^{-2}, respectively, relative to the baseline case. This partly offsets the effects of the decrease in aerosol emissions under the green recovery scenarios. In addition, under the fossil-fueled recovery scenario, there are persistent increases in the atmospheric contents of the WMGHGs that are the main contributors to the uptrend in the combined ERF.

Compared to the global annual mean, anthropogenic agents induce stronger ERFs at the region scale. Under the two green recovery scenarios, there are stronger positive ERFs over the middle latitudes of the NH and weak negative ERFs over the SH oceans over the period 2020–2050. The above positive ERFs are attributed to a sharp reduction in aerosols over the NH, whereas the negative ERFs come mainly from decreases in WMGHG ERFs over the SH oceans. These simultaneous decreases in WMGHG and aerosol emissions enhance the interhemispheric contrast of ERF by 0.5 (0.2–0.8) and 0.8 (0.7–0.9) W m^{-2}, respectively, relative to the baseline case. This is expected to further disturb cross-equatorial heat transport and rainfall distributions via oceanic processes and air-sea interactions (Broccoli et al., 2006; S. Y. Zhao & Suzuki, 2019). Conversely, the increases in WMGHG and aerosol emissions under the fossil-fueled recovery scenario lead to messy zonal changes in ERF and negligible changes in interhemispheric contrast of ERF, relative to the baseline case. This indicates that the contributions of increased anthropogenic emissions under this scenario to ERFs are limited to the local areas, as opposed to inducing further hemispheric differences. These regional changes in ERF are closely related to the cloud-cover changes that modify local radiation budgets by cloud radiative effects.

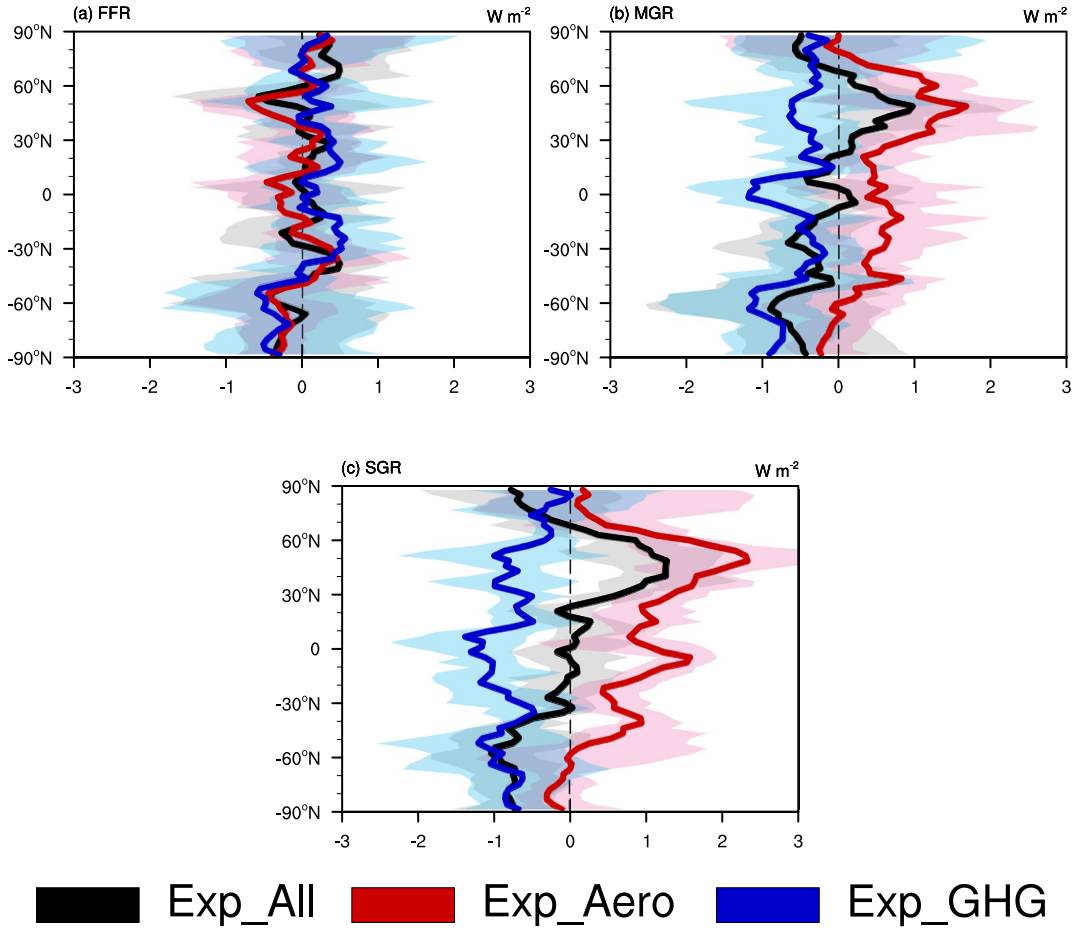

Figure 11. Zonal mean changes in the annual mean effective radiative forcings (ERFs; unit: W m^{-2}) over the period 2020–2050 under three Covid-19 economic recovery scenarios relative to the baseline case. The black, red, and blue lines represent the results from the Exp_All, Exp_Aero, and Exp_GHG group, respectively. The paler plumes show the spread of five ensemble members, whereas the solid lines represent their average results.

This study focuses primarily on the ERF contributed by anthropogenic emission changes as a result of Covid-19 containment and different post-pandemic emission policies. The individual contributions of each agent, such as the WMGHGs and aerosols, are assessed. This has certain implications for quantifying the impacts of the Covid-19 pandemic. However, the limitation in this study still needs to point out. First, the Covid-19 economic recovery scenarios are based on highly idealized assumptions regarding to investment in low-carbon sources and the resulting emission levels (Forster et al., 2020), which could lead to the uncertainty in the projections of future anthropogenic ERFs. Multi-model ensemble simulations are also required to avoid the uncertainty from the single-model simulation (Lamboll et al., 2021; Pincus et al., 2016; Weber et al., 2020). Additionally, previous studies have

Table 3
Interhemispheric Contrasts of the Annual Mean ERFs (unit: W m^{-2}) Over the Period 2020–2050 Under Three Covid-19 Economic Recovery Scenarios, Relative to the Baseline Case, in the Exp_All, Exp_Aero, and Exp_GHG Group

	Exp_All	Exp_Aero	Exp_GHG
Fossil-fueled recovery	0 (−0.2 to 0.2)	0 (−0.3 to 0.2)	0.1 (−0.2 to 0.5)
Moderate green recovery	0.5 (0.2–0.8)	0.3 (0–0.6)	0.1 (0–0.3)
Strong green recovery	0.8 (0.7–0.9)	0.6 (0.3–0.8)	0.2 (0.1–0.3)

Note. The values in parentheses represent the 5%–95% confidence range, and the positive values indicate that increases in ERF are larger at the NH than that in the SH.

pointed out the large reduction in emissions of short-lived gases induced by Covid-19 containment, such as nitrogen oxides and ozone (Goldberg et al., 2020; Keller et al., 2020; Venter et al., 2020), which are important contributors to anthropogenic ERF (Jones et al., 2021; Oshima et al., 2020; Weber et al., 2020). However, some of these anthropogenic agents are not discussed in this work. The aerosol ERFs could be a little bit underestimated under the Covid-19 green recovery scenarios due to the absence of contribution from nitrate aerosol ERF (An et al., 2019), whereas combined contribution of nitrogen oxides and ozone to the total anthropogenic ERF remains uncertainty due to the nonlinear relationship between them (Oshima et al., 2020; T. Wang et al., 2017). Z. L. Wang et al. (2021) showed that some widely adopted CMIP6 pathways, for example, the SSP2-4.5 scenario, underestimate the more recent decline in anthropogenic aerosol emissions over China. These overestimates of anthropogenic aerosol emissions are not corrected for the Covid-MIP scenarios, and the resulting aerosol ERFs could be a little be overestimated since the emission variations are applied on a percentage basis. Solving these problems will require more complex chemistry processes included (An et al., 2019), more trustworthy emission inventory (Paulot et al., 2018; Z. L. Wang et al., 2021), and more computing costs in the future. In this study, the contrasts in ERFs between the two hemispheres under the two green recovery scenarios are obvious due to the simultaneous decreases in WMGHG and aerosol emissions. The resulting climate responses to these reductions through slow oceanic processes and air-sea interactions should be further examined in future work.

Data Availability Statement

The SSP2-4.5 data sets were downloaded from the input data sets platform for model intercomparsion projects by searching "ScenarioMIP", "emissions", and "IAMC-MESSAGE-GLOBIOM-ssp245-1-1" on the download data page (Feng et al., 2020; Input4MIPs, 2020; https://esgf-node.llnl.gov/search/input4mips/). The historical multimodel ensemble simulations with all forcing from the Radiative Forcing Model Intercomparison Project (RFMIP-ERF-HistAll) were obtained from the Earth System Grid Federation by searching "RFMIP" and "piClim-histall" on the CMIP6 Search Interface (https://esgf-node.llnl.gov/search/cmip6). The concentration data sets of WMGHGs are accessible at https://github.com/Priestley-Centre/COVID19_emissions/.

Acknowledgments
This work was financially supported by the National Key R&D Program of China (2017YFA0603502), the (Key) National Natural Science Foundation of China (91644211), and S&T Development Fund of CAMS (2021KJ004 and 2022KJ019).

References

Alfaro, S. C., & Gomes, L. (2001). Modeling mineral aerosol production by wind erosion: Emission intensities and aerosol size distributions in source areas. *Journal of Geophysical Research: Atmospheres*, *106*(D16), 18075–18084. https://doi.org/10.1029/2000jd900339

An, Q., Zhang, H., Wang, Z. L., Liu, Y., Liu, Q. X., Wang, Z. Z., et al. (2019). The development of an atmospheric aerosol/chemistry-climate model, BCC_AGCM_CUACE2.0, and simulated effective radiative forcing of nitrate aerosols. *Journal of Advances in Modeling Earth Systems*, *11*, 3816–3835. https://doi.org/10.1029/2019MS001622

Andrijevic, M., Schleussner, C. F., Gidden, M. J., McCollum, D. L., & Rogelj, J. (2020). COVID-19 recovery funds dwarf clean energy investment needs. *Science*, *370*, 298–300. https://doi.org/10.1126/science.abc9697

Balkan Green Energy News. (2020). *EU cuts just transition fund to EUR 10 billion in COVID-19 recovery deal*. Retrieved from https://balkangreenenergynews.com/eu-cuts-just-transition-fund-to-eur-10-billion-in-covid-19-recovery-deal/

Broccoli, A. J., Dahl, K. A., & Stouffer, R. J. (2006). Response of the ITCZ to Northern Hemisphere cooling. *Geophysical Research Letters*, *33*(1), L01702. https://doi.org/10.1029/2005GL024546

Chiang, J. C. H., & Bitz, C. M. (2005). Influence of high latitude ice cover on the marine intertropical convergence zone. *Climate Dynamics*, *25*, 477–496. https://doi.org/10.1007/s00382-005-0040-5

Cubasch, U., Wuebbles, D., Chen, D., Facchini, M. C., Frame, D., Mahowald, N., et al. (2013). Introduction. In T. F.Stocker, D.Qin, G. K.Plattner, M.Tignor, S. K.Allen, J.Boschung, et al. (Eds.), *Climate change 2013: The physical science basis. Contribution of Working Group I to the Fifth Assessment Report of the Intergovernmental Panel on Climate Change*. Cambridge University Press.

European Commission. (2020). *Supporting climate action through the EU budget*. Retrieved from https://ec.europa.eu/clima/policies/budget/mainstreaming_en

Fadnavis, S., Sabin, T. P., Rap, A., Müller, R., Kubin, A., & Heinold, B. (2021). The impact of COVID-19 lockdown measures on the Indian summer monsoon. *Environmental Research Letters*, *16*(2021), 074054. https://doi.org/10.1088/1748-9326/ac109c

Fasullo, J. T., Rosenbloom, N., Buchholz, R. R., Danabasoglu, G., Lawrence, D. M., & Lamarque, J.-F. (2021). Coupled climate responses to recent Australian Wildfire and COVID-19 emissions anomalies estimated in CESM2. *Geophysical Research Letters*, *48*, e2021GL093841. https://doi.org/10.1029/2021GL093841

Feng, L., Smith, S. J., Braun, C., Crippa, M., Gidden, M. J., Hoesly, R., et al. (2020). The generation of gridded emissions data for CMIP6. *Geoscientific Model Development*, *13*, 461–482. https://doi.org/10.5194/gmd-13-461-2020

Fiedler, S., Stevens, B., Gidden, M., Smith, J. S., Riahi, K., & van Vuuren, D. (2019). First forcing estimates from the future CMIP6 scenarios of anthropogenic aerosol optical properties and an associated Twomey effect. *Geoscientific Model Development*, *12*, 989–1007. https://doi.org/10.5194/gmd-12-989-2019

Fiedler, S., Wyser, K., Rogelj, J., & van Noije, T. (2021). Radiative effects of reduced aerosol emissions during the COVID-19 pandemic and the future recovery. *Atmospheric Research*, *264*, 105866. https://doi.org/10.1016/j.atmosres.2021.105866

Forster, P. M., Forster, H. I., Evans, M. J., Gidden, M. J., Jones, C. D., Keller, C. A., et al. (2020). Current and future global climate impacts resulting from COVID-19. *Nature Climate Change*, *10*, 913–919. https://doi.org/10.1038/s41558-020-0883-0

Forster, P. M., Richardson, T., Maycock, A. C., Smith, C. J., Samset, B. H., Myhre, G., et al. (2016). Recommendations for diagnosing effective radiative forcing from climate models for CMIP6. *Journal of Geophysical Research: Atmosphere*, *121*, 12460–12475. https://doi.org/10.1002/2016JD025320

Fricko, O., Havlik, P., Rogelj, J., Klimont, Z., Gusti, M., Johnson, T., et al. (2016). The marker quantification of the shared socioeconomic pathway 2: A middle-of-the-road scenario for the 21st century. *Global Environmental Change*, *42*, 251–267. https://doi.org/10.1016/j.gloenvcha.2016.06.004

Gettelman, A., Lamboll, R., Bardeen, C. G., Forster, P. M., & Watson-Parris, D. (2020). Climate impacts of COVID-19 induced emission changes. *Geophysical Research Letters*, *48*, e2020GL091805. https://doi.org/10.1029/2020GL091805

Gettelman, A., Morrison, H., & Ghan, S. J. (2008). A new two-moment bulk stratiform cloud microphysics scheme in the community atmosphere model, version 3 (CAM3). Part II: Single-column and global results. *Journal of Climate*, *21*, 3660–3679. https://doi.org/10.1175/2008jcli2116.1

Gillingham, K. T., Knittel, C. R., Li, J., Ovaere, M., & Reguant, M. (2020). The short-run and long-run effects of Covid-19 on energy and the environment. *Joule*, *4*, 1337–1341. https://doi.org/10.1016/j.joule.2020.06.010

Goldberg, D. L., Anenberg, S. C., Griffin, D., McLinden, C. A., Lu, Z. F., & Streets, D. G. (2020). Disentangling the impact of the COVID-19 lockdowns on urban NO_2 from natural variability. *Geophysical Research Letters*, *47*(17), e2020GL089269. https://doi.org/10.1029/2020GL089269

Gong, S. L., Barrie, L. A., Blanchet, J. P., von Salzen, K., Lohmann, U., Lesins, G., et al. (2003). Canadian Aerosol Module: A size segregated simulation of atmospheric aerosol processes for climate and air quality models 1. Module development. *Journal of Geophysical Research: Atmospheres*, *108*(D1), 4007. https://doi.org/10.1029/2001jd002002

Gong, S. L., Barrie, L. A., & Lazare, M. (2002). Canadian Aerosol Module (CAM): A size-segregated simulation of atmospheric aerosol processes for climate and air quality models 2. Global sea-salt aerosol and its budgets. *Journal of Geophysical Research: Atmospheres*, *107*(D24), 4779. https://doi.org/10.1029/2001JD002004

Grandey, B. S., Rothenberg, D., Avramov, A., Jin, Q. J., Lee, H., Liu, X. H., et al. (2018). Effective radiative forcing in the aerosol-climate model CAM5.3-MARC-ARG. *Atmospheric Chemistry and Physics*, *18*(21), 15783–15810. https://doi.org/10.5194/acp-18-15783-2018

Heerwaarden, C. C., Mol, W. B., Veerman, M. A., Benedict, I., Heusinkveld, B. G., Knap, W. H., et al. (2021). Record high solar irradiance in Western Europe during first COVID-19 lockdown largely due to unusual weather. *Communications Earth & Environment*, *2*(1), 37. https://doi.org/10.1038/s43247-021-00110-0

Hepburn, C., O'Callaghan, B., Stern, N., Stern, N., & Stiglitz, J. (2020). *Will COVID-19 fiscal recovery packages accelerate or retard progress on climate change? Oxford review of economic policy* (pp. S359–S381). https://doi.org/10.1093/oxrep/graa015

Input4MIPs. (2020). The generation of gridded emissions data for CMIP6. [Dataset]. Earth System Grid Federation. Retrieved https://esgf-node.llnl.gov/search/input4mips/

Jing, X. W., Zhang, H., Peng, J., Li, J. N., & Barker, H. W. (2016). Cloud overlapping parameter obtained from CloudSat/CALIPSO data set and its application in AGCM with McICA scheme. *Atmospheric Research*, *170*(15), 52–65. https://doi.org/10.1016/j.atmosres.2015.11.007

Jones, C. D., Hickman, J. E., Rumbold, S. T., Walton, J., Lamboll, R. D., Skeie, R. B., et al. (2021). The climate response to emissions reductions due to COVID-19. *Geophysical Research Letters*, *48*(8), e2020GL091883. https://doi.org/10.1029/2020GL091883

Keller, C. A., Evans, M. J., Knowland, K. E., Hasenkopl, C. A., Modekurty, S., Lucchesi, R. A., et al. (2020). Global impact of COVID-19 restrictions on the atmospheric concentrations of nitrogen dioxide and ozone. *Atmospheric Chemistry and Physics Discussions*, 1–32. https://doi.org/10.5194/acp-2020-685

Keramidas, K., Fosse, F., Diaz-Vazquez, A., Schade, B., Tchung-Ming, S., Weitzel, M., et al. (2021). *Global Energy and Climate Outlook 2020: A new normal beyond Covid-19*. Publications Office of the European Union. https://doi.org/10.2760/608429

Lamboll, R. D., Jones, C. D., Skeie, R. B., Fiedler, S., Samset, B. H., Gillett, N. H., et al. (2021). Modifying emissions scenario projections to account for the effects of COVID-19: Protocol for Covid-MIP. *Geophysical Research Letters Discussions*, *14*(6), 3683–3695. https://doi.org/10.5194/gmd-14-3683-2021

Le Quéré, C., Jackson, R. B., Jones, M. W., Smith, A. J., Abernethy, S., Andrew, R. M., et al. (2020). Temporary reduction in daily global CO_2 emissions during the COVID-19 forced confinement. *Nature Climate Change*, *10*, 647–653. https://doi.org/10.1038/s41558-020-0797-x

Lewinschal, A., Ekman, A. M. L., Hansson, H. C., Sand, M., Berntsen, T. K., & Langner, J. (2019). Local and remote temperature response of regional SO_2 emissions. *Atmospheric Chemistry and Physics*, *19*, 2385–2403. https://doi.org/10.5194/acp-19-2385-2019

Li, J. D., Wang, W. C., Mao, J. Y., Wang, Z. Q., Zeng, G., & Chen, G. X. (2019). Persistent spring shortwave cloud circulations over southeastern China. *Journal of Climate*, *32*(11), 3069–3087. https://doi.org/10.1175/JCLI-D-18-0385.1

Liu, R. J., & Liao, H. (2017). Assessment of aerosol effective radiative forcing and surface air temperature response over eastern China in CMIP5 models. *Atmospheric and Ocean Science Letters*, *10*(3), 228–234. https://doi.org/10.1080/16742834.2017.1301188

Liu, Y. W., Zhang, K., Qian, Y., Wang, Y. H., Zou, Y. F., Song, Y. J., et al. (2018). Investigation of short-term effective radiative forcing of fire aerosols over North America using nudged hindcast ensembles. *Atmospheric Chemistry and Physics*, *18*(1), 31–47. https://doi.org/10.5194/acp-18-31-2018

Liu, Z., Ciais, P., Deng, Z., Lei, R. X., Davis, S. J., Zheng, B., et al. (2020). COVID-19 causes record decline in global CO2 emissions. Preprint at arXiv:2004.13614.

Lokhandwala, S., & Gautam, P. (2020). Indirect impact of COVID-19 on environment: A brief study in Indian context. *Environmental Research*, *188*, 109807. https://doi.org/10.1016/j.envres.2020.109807

Lund, M. T., Myhre, G., & Samset, B. H. (2019). Anthropogenic aerosol forcing under the shared socioeconomic pathways. *Atmospheric Chemistry and Physics*, *19*(22), 13827–13839. https://doi.org/10.5194/acp-19-13827-2019

Marticorena, B., & Bergametti, G. (1995). Modeling the atmospheric dust cycle: 1. Design of a soil-derived dust emission scheme. *Journal of Geophysical Research: Atmospheres*, *100*(D8), 16415–16430. https://doi.org/10.1029/95JD00690

Morrison, H., & Gettelman, A. (2008). A new two-moment bulk stratiform cloud microphysics scheme in the Community Atmosphere Model, version 3 (CAM3). Part I: Description and numerical tests. *Journal of Climate*, *21*(15), 3642–3659. https://doi.org/10.1175/2008JCLI2105.1

Mulcahy, J. P., Jones, C., Sellar, A., Johnson, B., Boutle, I. A., Jones, A., et al. (2018). Improved aerosol processes and effective radiative forcing in HadGEM3 and UKESM1. *Journal of Advances in Modeling Earth Systems*, *10*(11), 2786–2805. https://doi.org/10.1029/2018ms001464

Myhre, G., Myhre, C. E. L., Samset, B., & Storelvmo, T. (2013). Aerosols and their relation to global climate and climate sensitivity. *Nature Education Knowledge*, *4*(5), 7.

Myhre, G., Samset, B. H., Schulz, M., Balkanski, Y., Bauer, S., Berntsen, T. K., et al. (2013). Radiative forcing of the direct aerosol effect from AeroCom Phase II simulations. *Atmospheric Chemistry Physics*, *13*, 1853–1877. https://doi.org/10.5194/acp-13-1853-2013

Myhre, G., Shindell, D., Bréon, F.-M., Collins, W., Fuglestvedt, J., Huang, J., et al. (2013). Anthropogenic and natural radiative forcing. In T. F.Stocker, D.Qin, G.-K.Plattner, M.Tignor, S. K.Allen, J.Boschung, et al. (Eds.), *Climate change 2013: The physical science basis. Contribution of Working Group I to the Fifth Assessment Report of the Intergovernmental Panel on Climate Change*. Cambridge University Press.

Nakajima, T., Tsukamoto, M., Tsushima, Y., Numagui, A., & Kimura, T. (2000). Modeling of the radiative process in an atmospheric general circulation model. *Applied Optics*, *39*(27), 4869. https://doi.org/10.1364/ao.39.004869

O'Neill, B. C., Tebaldi, C., van Vuuren, D. P., Eyring, V., Friedlingstein, P., Hurtt, G., et al. (2016). The Scenario Model Intercomparison Project (ScenarioMIP) for CMIP6. *Geoscientific Model Development*, *9*(9), 3461–3482. https://doi.org/10.5194/gmd-9-3461-2016

Oshima, N., Yukimoto, S., Deushi, M., Koshiro, T., Kawai, H., Tanaka, T. Y., et al. (2020). Global and Arctic effective radiative forcing of anthropogenic gases and aerosols in MRI-ESM2.0. *Progress in Earth and Planetary Science*, *7*(1), 1–21. https://doi.org/10.1186/s40645-020-00348-wcheck doi

Paulot, F., Paynter, D., Ginoux, P., Naik, V., & Horowitz, L. W. (2018). Changes in the aerosol direct radiative forcing from 2001 to 2015: Observational constraints and regional mechanisms. *Atmospheric Chemistry and Physics*, *18*, 13265–13281. https://doi.org/10.5194/acp-18-13265-2018

Peters, I. M., Brabec, C., Buonassisi, T., Hauch, J., & Nobre, A. M. (2020). The impact of COVID-19-related measures on the solar resource in areas with high levels of air pollution. *Joule*, *4*(8), 1681–1687. https://doi.org/10.1016/j.joule.2020.06.009

Pincus, R., Forster, P. M., & Bjorn, S. (2016). The Radiative Forcing Model Intercomparison Project (RFMIP): Experimental protocol for CMIP6. *Geoscientific Model Development*, *9*(9), 3447–3460. https://doi.org/10.5194/gmd-9-3447-2016

Qian, L. H., Fang, Q., & Lu, Z. W. (2020). *The theme of economic recovery: "green" and "digital"*(in Chinese). Retrieved from https://mp.weixin.qq.com/s/JdlekUCT2wWLynydOwcbTw

Ren, L., Yang, Y., Wang, H., Zhang, R., Wang, P., & Liao, H. (2020). Source attribution of Arctic black carbon and sulfate aerosols and associated Arctic surface warming during 1980–2018. *Atmospheric Chemistry and Physics*, *20*, 9067–9085. https://doi.org/10.5194/acp-20-9067-2020

Riahi, K., van Vuuren, D. P., Kriegler, E., Kriegler, E., O'Neill, B. C., Fujimori, S., et al. (2016). The Shared Socioeconomic Pathways and their energy, land use, and greenhouse gas emissions implications: An Overview. *Global Environmental Change*, *42*, 153–168. https://doi.org/10.1016/j.gloenvcha.2016.05.009

Röser, F., Widerberg, O., Höhne, N., & Day, T. (2020). Ambition in the making: Analyzing the preparation and implementation process of the Nationally Determined contributions under the Paris Agreement. *Climate Policy*, *20*(4), 415–429. https://doi.org/10.1080/14693062.2019.1708697

Schneider, T., Bischoff, T., & Haug, G. H. (2014). Migrations and dynamics of the intertropical convergence zone. *Nature*, *513*, 45–53. https://doi.org/10.1038/nature13636

Smith, C. J., Kramer, R. J., Myhre, G., Alterskjaer, K., Collins, W., Sima, A., et al. (2020). Effective radiative forcing and adjustments in CMIP6 models. *Atmospheric Chemistry and Physics*, *20*, 9591–9618. https://doi.org/10.5194/acp-20-9591-2020

Smith, C. J., Kramer, R. J., Myhre, G., Forster, P. M., Soden, B., Andrews, T., et al. (2018). Understanding rapid adjustments to diverse forcing agents. *Geophysical Research Letters*, *45*(12), 12023–12031. https://doi.org/10.1029/2018GL079826

Tang, T., Shindell, D., Faluvegi, G., Myhre, G., Olivié, D., Voulgarakis, A., et al. (2019). Comparison of effective radiative forcing calculations using multiple methods, drivers, and models. *Journal of Geophysical Research: Atmospheres*, *124*, 4382–4394. https://doi.org/10.1029/2018JD030188

Tolliver, C., Keeley, A. R., & Managi, S. (2020). Drivers of green bond market growth: The importance of Nationally Determined contributions to the Paris Agreement and implications for sustainability. *Journal of Cleaner Production*, *244*, 118643. https://doi.org/10.1016/j.jclepro.2019.118643

Tsigaridis, K., Daskalakis, N., Kanakidou, M., Adams, P. J., Artaxo, P., Bahadur, R., et al. (2014). The AeroCom evaluation and intercomparison of organic aerosol in global models. *Atmospheric Chemistry and Physics*, *14*(5), 6027–6161. https://doi.org/10.5194/acp-14-10845-2014

United Nations Environment Programme. (2020). *Emissions Gap Report 2020*. Retrieved from https://www.unep.org/emissions-gap-report-2020

United Nations Environment Programme. (2021). *Emissions Gap Report 2021*.Retrieved from https://www.unep.org/emissions-gap-report-2021

Venter, Z. S., Aunan, K., Chowdhury, S., & Lelieveld, J. (2020). COVID-19 lockdowns cause global air pollution declines. *Proceedings of the National Academy of Sciences of the United States of America*, *117*(32), 18984–18990. https://doi.org/10.1073/pnas.2006853117

Wang, H., Dai, T., Zhao, M., Goto, D., Bao, Q., Takemura, T., et al. (2020). Aerosol effective radiative forcing in the online aerosol coupled CAS-FGOALS-f3-L climate model. *Atmosphere*, *11*(10), 1115. https://doi.org/10.3390/atmos11101115

Wang, T., Xue, L. K., Brimblecombe, P., Lam, Y. F., Li, L., & Zhang, L. (2017). Ozone pollution in China: A review of concentrations, meteorological influences, chemical precursors, and effects. *Science of the Total Environment*, *575*, 1582–1596. https://doi.org/10.1016/j.scitotenv.2016.10.081

Wang, Z. L., Lin, L., Xu, Y. Y., Che, H. Z., Zhang, X. Y., Zhang, H., et al. (2021). Incorrect Asian aerosols affecting the attribution and projection of regional climate change in CMIP6 models. *npj Climate and Atmospheric Science*, *4*(2). https://doi.org/10.1038/s41612-020-00159-2

Wang, Z. L., Lin, L., Yang, M. L., & Xu, Y. Y. (2016). The effect of future reduction in aerosol emissions on climate extremes in China. *Climate Dynamics*, *47*, 2885–2899. https://doi.org/10.1007/s00382-016-3003-0

Wang, Z. L., Zhang, H., & Lu, P. (2014). Improvement of cloud microphysics in the aerosol-climate model BCC_AGCM2.0.1_CUACE/Aero, evaluation against observations, and updated aerosol indirect effect. *Journal of Geophysical Research: Atmospheres*, *119*, 8400–8417. https://doi.org/10.1002/2014JD021886

Weber, J., Shin, Y. M., Sykes, J. S., Archer-Nicholls, S., Abranham, N. L., & Archibald, A. T. (2020). Minimal climate impacts from short-lived climate forcers following emission reductions related to the COVID-19 pandemic. *Geophysical Research Letters*, *47*(20). https://doi.org/10.1029/2020GL090326

Wei, X. D., & Zhang, H. (2011). Analysis of optical properties of nonspherical dust-like aerosols. *Acta Optica Sinica*, *31*(5), 0501002. https://doi.org/10.3788/aos201131.0501002

Westervelt, D. M., Horowitz, L. W., Naik, V., Golaz, J. C., & Mauzerall, D. L. (2015). Radiative forcing and climate response to projected 21st century aerosol decreases. *Atmospheric Chemistry and Physics*, *15*(22), 12681–12703. https://doi.org/10.5194/acp-15-12681-2015

Wu, T. W., Yu, R. C., Zhang, F., Wang, Z. Z., Dong, M., Wang, L. N., et al. (2010). The Beijing climate center atmospheric general circulation model: Description and its performance for the present-day climate. *Climate Dynamic*, *34*, 123–147. https://doi.org/10.1007/s00382-008-0487-2

Xie, B., Zhang, H., Yang, D. D., & Wang, Z. L. (2016). A modeling study of effective radiative forcing and climate response due to increased methane concentration. *Advances in Climate Change Research*, *7*(4), 241–246. https://doi.org/10.1016/j.accre.2016.12.001

Yang, D. D., Zhang, H., & Li, J. N. (2019). Changes in anthropogenic $PM_{2.5}$ and the resulting global climate effects under the RCP4.5 and RCP8.5 scenarios by 2050. *Earth's Future*, *8*(1), e2019EF001285. https://doi.org/10.1029/2019ef001285

Yang, Y., Ren, L. L., Li, H. M., Wang, H. L., Wang, P. Y., Chen, L., et al. (2020). Fast climate responses to aerosol emission reductions during the COVID-19 pandemic. *Geophysical Research Letters*, *47*, e2020GL089788. https://doi.org/10.1029/2020gl089788

Yang, Y., Ren, L., Wu, M., Wang, H., Song, F., Leung, L. R., et al. (2022). Abrupt emissions reductions during COVID-19 contributed to record summer rainfall in China. *Nature Communications*, *13*, 959. https://doi.org/10.1038/s41467-022-28537-9

Yang, Y., Smith, S. J., Wang, H., Mills, C. M., & Rasch, P. J. (2019). Variability, timescales, and nonlinearity in climate responses to black carbon emissions. *Atmospheric Chemistry and Physics*, *19*, 2405–2420. https://doi.org/10.5194/acp-19-2405-2019

Zhang, H., Chen, Q., & Xie, B. (2015). A new parameterization for ice cloud optical properties used in BCC-RAD and its radiative impact. *Journal of Quantitative Spectroscopy and Radiative Transfer*, *150*, 76–86. https://doi.org/10.1016/j.jqsrt.2014.08.024

Zhang, H., Jing, X. W., & Li, J. (2014). Application and evaluation of a new radiation code under McICA scheme in BCC_AGCM2.0.1. *Geoscientific Model Development*, *7*, 737–754. https://doi.org/10.5194/gmd-7-737-2014

Zhang, H., Shen, Z. P., Wei, X., Zhang, M., & Li, Z. (2012). Comparison of optical properties of nitrate and sulfate aerosol and the direct radiative forcing due to nitrate in China. *Atmospheric Research*, *113*, 113–125. https://doi.org/10.1016/j.atmosres.2012.04.020

Zhang, H., Wang, Z. L., Wang, Z. Z., Liu, Q. X., Gong, S. L., Zhang, X. Y., et al. (2012). Simulation of direct radiative forcing of typical aerosols and their effects on global climate using an online AGCM-aerosol coupled model system. *Climate Dynamics*, *38*, 1675–1693. https://doi.org/10.1007/s00382-011-1131-0

Zhang, H., Xie, B., & Wang, Z. L. (2018). Effective radiative forcing and climate response to short-lived climate pollutants under different scenarios. *Earth's Future*, *6*(6), 857–866. https://doi.org/10.1029/2018EF000832

Zhang, H., Zhao, S. Y., Wang, Z. L., Zhang, X. Y., & Song, L. C. (2016). The updated effective radiative forcing of major anthropogenic aerosols and their effects on global climate at present and in the future. *Journal of Climatology*, *36*(12), 4029–4044. https://doi.org/10.1002/joc.4613

Zhao, A., Stevenson, D. S., & Bollasina, M. A. (2019). Climate forcing and response to greenhouse gases, aerosols, and ozone in CESM1. *Journal of Geophysical Research: Atmospheres*, *124*(24). https://doi.org/10.1029/2019JD030769

Zhao, S. Y., & Suzuki, K. (2019). Differing impacts of black carbon and sulfate aerosols on global precipitation and the ITCZ location via atmosphere and Ocean energy perturbations. *Journal of Climate*, *32*(17), 5567–5582. https://doi.org/10.1175/jcli-d-18-0616.1

Zheng, H., Kong, S., Chen, N., Yan, Y. Y., Liu, D. T., Zhu, B., et al. (2020). Significant changes in the chemical compositions and sources of $PM_{2.5}$ in Wuhan since the city lockdown as COVID-19. *Science of the Total Environment*, *739*, 140000. https://doi.org/10.1016/j.scitotenv.2020.140000

Zhou, C., Zhang, H., Zhao, S. Y., & Li, J. N. (2017). On effective radiative forcing of partial internally and externally mixed aerosols and their effects on global climate. *Journal of Geophysical Research: Atmospheres*, *123*(1), 401–423. https://doi.org/10.1002/2017JD027603

Zhou, C. H., Gong, S., Zhang, X. Y., Liu, H. L., Xue, M., Cao, G. L., et al. (2012). Towards the improvements of simulating the chemical and optical properties of Chinese aerosols using an online coupled model—CUACE/Aero. *Tellus B: Chemical and Physical Meteorology*, *64*(1), 91–102. https://doi.org/10.3402/tellusb.v64i0.18965

Zhou, T. J., Chen, X. L., Dong, L., Wu, B., Man, W. M., Zhang, L. X., et al. (2014). Chinese contribution to CMIP5: An overview of five Chinese Model's performances. *Journal of Meteorological Research*, *28*(4), 481–509. https://doi.org/10.1007/s13351-014-4001-y

Zhou, T. J., Zou, L. W., Wu, B., Jin, C. X., Song, F. F., Chen, X. L., et al. (2014). Development of earth/climate system models in China: A review from the Coupled Model Intercomparison Project perspective. *Journal of Meteorological Research*, *28*(5), 762–779. https://doi.org/10.1007/s13351-014-4501-9